| Title | Computational study on the effects of central retinal blood vessels with asymmetric geometries on optic nerve head biomechanics |
|---|---|
| Author(s) | Otani, Tomohiro; Miyata, Kota; Miki, Atsuya et al. |
| Citation | Medical Engineering and Physics. 2024, 123, p. 104086 |
| Version Type | AM |
| URL | https://hdl.handle.net/11094/93456 |
| rights | © 2024. This manuscript version is made available under the CC-BY-NC-ND 4.0 license https://creativecommons.org/licenses/by-nc-nd/4.0/ |
| Note | |

**Computational study on the effects of central retinal blood vessels with asymmetric geometries on optic nerve head biomechanics**

1   Tomohiro Otani[a,*], Kota Miyata[a], Atsuya Miki[b], Shigeo Wada[a]

2

3   a.   *Department of Mechanical Science and Bioengineering, Graduate School of Engineering Science,*

4        *Osaka University*

5   b.   *Department of Myopia Control Research, Aichi Medical University*

6

7

8   Type: Original Article

9

10   * Corresponding author at:

11   Tomohiro Otani, PhD

12   Department of Mechanical Science and Bioengineering,

13   Graduate School of Engineering Science, Osaka University

14   1-3 Machikaneyamacho, Toyonaka, Osaka, 560-8531, Japan

15   Phone: +81-6-6850-6174

16   E-mail: otani.tomohiro.es@osaka-u.ac.jp

17

18

19

20

21

**ABSTRACT**

Optic nerve head (ONH) biomechanics are associated with glaucoma progression and have received considerable attention. Central retinal vessels (CRVs) oriented asymmetrically in the ONH are the single blood supply source to the retina and are believed to act as mechanically stable elements in the ONH in response to intraocular pressure (IOP). However, these mechanical effects are considered negligible in ONH biomechanical studies and received less attention. This study investigated the effects of CRVs on ONH biomechanics taking into consideration three-dimensional asymmetric CRV geometries. A CRV geometry was constructed based on CRV centerlines extracted from optical coherence tomography ONH images in eight healthy subjects and superimposed in the idealized ONH geometry established in previous studies. Mechanical analyses of the ONH in response to the IOP were conducted in the cases with and without CRVs for comparison. Obtained results demonstrated that the CRVs induced anisotropic ONH deformation, particularly in the lamina cribrosa and the associated upper neural tissues (prelamina) with wide ranges of spatial strain distributions. These results indicated that the CRVs result in anisotropic deformation with local strain concentration, rather than function to mechanically support in response to the IOP as in the conventional thinking in ophthalmology.

Word count: 5184

## 1. Introduction

The optic nerve head (ONH) located on the posterior side of the eyeball is the region where retinal nerve fibers and blood vessels enter/exit the eyeball through the lamina cribrosa (LC), which is a disc-shaped porous tissue. Fine retinal nerve axons pass through pores of the LC, whereas a pair of a single retinal artery and vein pass through the LC and is composed of four main branches in each artery and vein (central retinal vessels: CRVs). Pathological alteration of the ONH tissues is associated with glaucoma, which is the second leading cause of vision loss [1]. Although comprehensive mechanisms of glaucoma progression remain unclear, ONH biomechanics is considered to be one of the essential associated factors [2–4].

In clinical practice, CRV morphological characteristics have received much attention as a biomarker of glaucoma progression [5,6]. The CRVs under healthy conditions pass through the LC slightly to the nasal side from the center of the LC and bifurcate to four main branches in the prelaminar domain. Because the CRVs may be relatively stiffer than neural fibers in the prelamina, they are believed to act as mechanically stable elements against mechanical deformation under normal conditions [7,8]. Whereas, positional shifts of the CRVs to the nasal side are commonly known from fundus photographs in glaucoma patients [6,9,10] and recent three-dimensional (3D) optical coherence tomography (OCT) imaging [11,12]. Although causal mechanisms of this nasal shift in glaucoma progression are still under debate, mechanical balances between the CRVs and ONH tissues damaged in glaucoma is a leading hypothesis [5,7,13]. Therefore, the mechanical implications of the effects of the CRVs on ONH biomechanics have attracted attention in ophthalmology.

However, the effects of the CRVs on ONH biomechanics have been considered to be negligible and received less attention in more recent biomechanical studies. Biomechanical studies considering ONH complex geometries originated with the pioneering study of [14] using an idealized axisymmetric ONH model, and this ONH model has become one of the generic models capable of representing complex multiple tissues constituting the ONH (e.g., applied for whole eyeball modeling [15]). Here, the CRVs were modeled as a single straight tube assigned on the central axis of the axisymmetric ONH model, and they concluded that the effects of the CRV on ONH biomechanics were weak except for some local stress concentrations [14]. Subsequent studies followed this proposal and investigated ONH biomechanics while overlooking CRV effects, for example, [15–18]. Nevertheless, the CRVs have 3D asymmetric geometries, and

3

72    the above simplification may underestimate their mechanical effects. Sigal et al., (2004) also noted this

73    concern and suggested further considerations regarding 3D CRV morphologies. As a first step to reveal the

74    mechanical effects of the CRVs on ONH biomechanics, the mechanical model of the ONH with CRVs should

75    be reconsidered, taking into consideration these 3D asymmetric geometries.

76          This study aimed to investigate potential CRV effects on ONH biomechanics taking into

77    consideration the asymmetric 3D CRV geometry. Consequently, we developed an asymmetric CRV

78    geometry based on CRV centerlines extracted from OCT imaging of the ONH in healthy normal subjects and

79    superimposed this geometry on an idealized axisymmetric ONH model. Computational mechanical

80    simulations of the ONH against intraocular pressure (IOP) were conducted and the CRV effects on the

81    resultant deformed states of the ONH were evaluated.

82

83    **2. Methods**

84    *2.1. CRV geometry acquisition*

85          A CRV geometry taking into consideration anatomical morphologies was constructed based on the

86    OCT images of the ONH of eight participants. The participants were retrospectively enrolled from healthy

87    control subjects who underwent ophthalmologic examinations at the Osaka University Health and

88    Counseling Center as a regular health check-up. Patients with intraocular diseases except for cataracts, best-

89    corrected visual acuity worse than 0.5, the use of IOP-lowering medication, poor quality OCT images, or a

90    history of elevated IOP were excluded. A commercially available SS-OCT device (DRI-OCT, Topcon, Tokyo,

91    Japan) was used to acquire $6 \times 6$-mm$^2$ volume scans of the peripapillary area. Eyes were imaged using the

92    3D scan mode, for which the A-scan density was 512 lines (horizontal) × 256 lines (vertical), within a scan

93    time of 1.3 seconds. We applied a method we previously developed for deep learning-based noise reduction

94    of volumetric OCT scans [19]. The OCT images were reconstructed in a series of sagittal plane images in an

95    8-bit format. The in-plane pixel dimensions were $11.7 \times 2.57$ μm$^2$ and the slice thickness was 23.4 μm. The

96    study was approved by the Institutional Review Board of Osaka University (No. 18357). Volunteers gave

97    their oral and written informed consent.

4

98    The overall workflow of the CRV geometry acquisition is presented in Fig. 1. The CRV regions in the

99    OCT images (Fig. 1(a)) were clarified using the 3D line enhancement filter [20] implemented in the Insight

100   toolkit library [21] (Fig. 1(b)), and segmented based on image intensities with manual correction using

101   Mimics 24.0 (Materialise, Inc., Yokohama, Japan) referring to fundus photographs of each subject (Fig. 1(c)).

102   The CRV centerlines were extracted using a vascular modeling toolkit (VMTK 1.4.0, http://www.vmtk.org/),

103   and locations of the first and second branches and roots on the LC were obtained from the CRV centerlines.

104   To remove the subject-specific size differences, these positions were normalized using local coordinates, in

105   which the center of the LC top was set as the origin and the LC diameter was set to 1. An approximate shape

106   of the asymmetric CRV geometries was obtained from the averages (Fig. 1(d)).

107

108   *2.2. Modeling of the ONH with CRVs*

109   An idealized ONH geometry consisting of the LC, prelamina (anterior neural tissues on the LC), sclera,

110   and retina (Fig. 2(a)) was constructed using Rhinoceros 7.0 (Robert McNeel & Associates. Inc, Seattle, WA)

111   following design parameters shown in [22], except for the curvature of the eyeball. Here, we modeled the

112   computational domain as flat as in [23,24] to reduce the computational cost, and the sclera around the

113   ONH was cut as a square shape with an edge length of 4×LC diameter. The CRV centerlines constructed in

114   section 2.1 were also superimposed into the ONH [25], and the CRVs were modeled as closed cylinders for

115   simplicity. The diameter of the central retinal artery and vein were set to 0.154 mm and 0.179 mm,

116   respectively [26] and vessels after the second branch on the sclera and LC bottom was created by adding

117   straight tubes with the same respective diameters.

118

119   *2.3. Computational simulations*

120   Computational simulations using the ONH model with and without CRVs were conducted and these

121   deformation states were compared to evaluate the effects of the CRVs. The ONH shapes were discretized

122   as a set of tetrahedral meshes with a base mesh size of 0.15 mm using HyperMesh (Altair Engineering Inc.,

123   Troy, MI). We adopted the edge-based gradient smoothing technique in the smoothed finite element

124   method framework [27–29] to improve the computational accuracies (for more details of smoothed finite

5

125   element method, please see *supplementary material* 1), and solved the mechanical equilibrium equation

126   with respect to displacement vectors **u** in a finite element manner. Computational simulations were

127   conducted using an in-house smoothed finite element method solver and the linear algebraic equation was

128   solved using PARDISO implemented in the Intel oneAPI Math Kernel Library.

129   ONH tissues were modeled as isotropic nearly incompressible materials with linear elastic properties

130   and these material parameters were taken from [30], as summarized in Table 1. Boundary conditions were

131   illustrated in Fig. 3. An IOP of 20 mmHg [30] was loaded on the top surface of the ONH region, as a normal

132   range (<21 mmHg) [31]. We assumed that the eyeball deformation under IOP is isotropic and the resulting

133   in-plane deformation of the sclera around the ONH is also symmetric. To express this symmetric

134   deformation efficiently in computation, the sliding boundary condition was set on a pair of cross-sectional

135   planes (temporal and inferior planes, $\Omega_{x-}$ and $\Omega_{y-}$ in Fig. 3), and a circumferential (hoop) stress estimated

136   as 20 × IOP following [23] was loaded on another pair of cross-sectional planes (nasal and superior planes,

137   $\Omega_{x+}$ and $\Omega_{y+}$ in Fig. 3). To express the symmetric deformation against the hoop stress avoiding effects of

138   artificially set boundaries, each surface normal displacement on the $\Omega_{x+}$ and $\Omega_{y+}$ planes was constrained as

139   being uniform by the Lagrange multiplier method. Here, these geometric constraint conditions are given by

140
$$\mathbf{u} \cdot \mathbf{n} = U_{x+} \text{ on } \Omega_{x+}, \ \mathbf{u} \cdot \mathbf{n} = U_{y+} \text{ on } \Omega_{y+}, \tag{1}$$

141   where **n** is the unit surface normal, and $U_{x+}$ and $U_{y+}$ are the uniform surface normal displacement on $\Omega_{x+}$

142   and $\Omega_{y+}$, respectively. In addition, superior-inferior displacement was fixed on the bottom edges of the

143   cross-sectional planes.

144   As preliminary analyses, mesh size sensitivities were tested using ONH geometry with CRVs with

145   three different mesh sizes (fine: 0.075 mm, medium: 0.15 mm, and coarse: 0.3 mm) and conducted

146   computational simulation as the above conditions. Displacements along the central axis of the ONH were

147   compared among three cases and we confirmed that differences among the three cases were within 3%.

148   Therefore, we concluded that a medium size was appropriate for this study.

149

150   *2.4. Evaluation indices*

6

151    The ONH deformation in response to the IOP was evaluated by the first principal strain and

152    associated principal direction. Furthermore, the extent of deformation anisotropy was evaluated by

153    following two evaluation indices proposed by [32] using principal stretches $\lambda_i$ ($i$=1,2,3). Amelon et al., (2011)

154    proposed the anisotropic deformation index (ADI), given by

$$\text{ADI} = \left( \left( \frac{\lambda_1 - \lambda_2}{\lambda_2} \right)^2 + \left( \frac{\lambda_2 - \lambda_3}{\lambda_3} \right)^2 \right)^{\frac{1}{2}}. \tag{2}$$

156    ADI ranges from 0 to infinity and 0 means perfectly isotropic deformation ($\lambda_1 = \lambda_2 = \lambda_3$). Furthermore, to

157    distinguish the one-direction dominant (rod-like) and two-direction dominant (slab-like) deformations, the

158    slab-rod index (SRI) was defined as

$$\text{SRI} = \frac{\tan^{-1} \left( \lambda_3 \left( \lambda_1 - \lambda_2 \right) / \lambda_2 \left( \lambda_2 - \lambda_3 \right) \right)}{\pi/2}. \tag{3}$$

160    SRI ranges from 0 to 1, and 0 and 1 mean perfectly slab-like and rod-like deformations, respectively. Fig. 4

161    shows a schematic illustration of the meanings of the ADI and SRI.

162

163    **3. Results**

164        First, we compared the global deformation characteristics of the entire computational domain

165    with and without CRVs to evaluate the effects of artificially set boundaries and CRVs as a preliminary

166    confirmation. Both the surface normal displacements $U_{x+}$ and $U_{y+}$ were 4×10$^{-2}$ mm symmetrically and

167    differences resulting from the CRVs were <1×10$^{-3}$ mm, and thus we concluded that the computation

168    satisfactorily expressed the symmetric deformation of the entire computational domain against the IOP

169    regardless of the CRVs. Following this confirmation, we evaluated each deformation state of the ONH

170    components (sclera, LC, and prelamina) with and without CRVs, as follows.

171        Fig. 5 (a) shows the first principal strain on the cross-sectional plane of the sclera in the case of

172    CRVs. The strain was axisymmetrically distributed regardless of the CRVs and concentrated along the LC

173    boundaries, in which the principal stretches were oriented along circumferential directions. Fig. 5 (b), (c),

174    and (d) show the volume fractions of the first principal strain, ADI, and SRI, respectively. Each value showed

175     excellent agreement between the cases with and without CRVs. The strain was almost <0.02 and the ADI

176     ranged from 0.01 to 0.02. The volume fraction of the SRI had a maximum at an SRI of 0.01 and gradually

177     decreased with increasing SRI.

178         Fig. 6 (top and middle) shows the spatial distribution of the first principal strain, ADI, and SRI on

179     the central cross-sectional plane of the superior-inferior direction in the LC without and with CRVs. The

180     strain values distributed axisymmetrically in the case without CRVs, while local strain concentration

181     appeared around the CRVs in the case with CRVs. The extents of the anisotropic deformations were also

182     locally different in the ADI and SRI. With respect to the volume fractions of these values (Fig. 6 bottom),

183     these values were in good agreement between the case with and without CRVs while the volume fractions

184     of relatively higher values of both the ADI and SRI in the case with CRVs were larger than those in the case

185     without CRVs. To consider the LC global deformation, we visualized the first principal strain orientations in

186     the cross-sectional planes of the anterior-posterior direction in the LC (Fig. 7). Although circumferential

187     stretch was found on the upper plane in both cases with and without CRVs, the principal stretch orientations

188     displayed a different profile in the middle plane. The stretch orientation was axisymmetric in the case

189     without CRV, whereas strain oriented starting from the CRVs and displayed spatially asymmetric profiles.

190     The values of the strain were locally higher around the CRVs and these strain concentrations were more

191     prominent in the bottom regions.

192         Lastly, the spatial distribution of the first principal strain, ADI, and SRI on the cross-sectional plane

193     in the prelamina without and with CRVs were visualized (Fig. 8 top and middle). The strain was uniformly

194     distributed from 0.01 to 0.02 in the prelamina except for the top surface in the case without CRVs. By

195     contrast, the strain was locally higher and lower around the CRVs in the case with CRVs and ranged from 0

196     to 0.05. The ADI was locally lower around the CRVs, whereas the SRI was locally higher. Regarding the

197     volume fractions of these values (Fig. 8 bottom), the case with CRVs had much higher strain regions

198     compared with the case without CRVs. Clear differences between the cases with and without CRVs were

199     also found in the ADI and SRI. In particular, the SRI was nearly zero in almost all regions in the case without

200     CRVs, whereas in the case with CRVs, was relatively widely distributed.

201

**4. Discussion**

The clinical importance of CRV geometry in the ONH and its mechanical implications associated with glaucoma progression remain actively discussed in recent ophthalmic research [5,7,12,33], while CRV mechanical effects have been considered to be negligible in biomechanical studies of the ONH in the last two decades. To address this difference in opinion, the present study reconsidered the CRV mechanical effects on ONH biomechanics by computational analyses, taking into consideration the CRV geometries. The obtained results demonstrated that scleral deformation was in excellent agreement between the cases with and without CRVs, whereas the local deformation characteristics in the ONH, particularly in the LC and prelamina, displayed clear differences with the CRVs. These results may provide new important insights into the CRV effects on ONH biomechanics, as follows.

In the prelamina, the CRVs caused anisotropic deformations and the strain ranged widely, with high strain concentration compared to the case without CRVs (Fig. 8). In the case without CRVs, deformed axisymmetric and slab-like stretching (SRI≈0) was found, whereas anisotropic deformation with relatively rod-like stretching was found in the case with CRVs. These results indicated that the CRV leads to regionally different deformation with high strain concentration, rather than relieving the mechanical deformation by the IOP as in the conventional understanding in ophthalmology [7]. This finding may be interpreted by the following two reasons from mechanical viewpoints. One is that the CRV effects on the scleral deformation were negligible (Fig. 5), and the total extent of the resultant in-plane deformation of the prelamina was similarly not influenced by the CRVs. Because the in-plane deformation by the hoop stress originating from the IOP is dominant in ONH deformation [23], the CRV may not provide sufficient mechanical resistance to ONH deformations. Another reason is that the CRVs are located within soft tissues of the ONH, the ONH itself not being attached to any other stiffer tissues other than the CRVs for fixation, and thus the CRVs may not act as reinforcement components of the ONH, instead disturbing the axisymmetric, uniform distributions of the prelamina. These new insights potentially update the conventional understanding of the mechanical implication of the CRVs in ophthalmology.

Not only the prelamina, but also the LC deformation states were influenced by the CRVs (Figs. 6 and 7). Although the strain ranges and extents of anisotropic deformations were secondary compared to

229    the prelamina (Fig. 6), the principal strain direction was not axisymmetric in the case with the CRVs and the

230    strain oriented starting from the CRVs due to the relatively stiffer material properties of the CRVs. It is well

231    established that the CRVs are located nasally in the human ONH [7], and thus the asymmetric deformation

232    of the LC due to the presence of CRVs, as observed from the obtained results, is anatomically reasonable.

233    Furthermore, mechanical damage of the LC in glaucoma patients is widely known and the extent of this

234    damage displays regional differences [34,35]. Although the CRV effects on the extent of the degree of strain

235    are secondary in this study assuming healthy subjects, these effects on ONH mechanics might become

236    greater in glaucoma patients with regionally deteriorated mechanical properties in the LC.

237         This study has three main limitations. First, mechanical analyses of the subject-specific ONH with

238    actual CRV geometries were still challenging due to the limits of the spatial resolution of the *in vivo* OCT

239    imaging. In particular, quantitative evaluations of cross-sectional shapes of the CRVs, particularly

240    intersecting regions between the artery and vein [36], are difficult to extract from OCT images, and thus we

241    assumed these shapes as closed cylinders. Although the mechanical simulation using anatomically

242    consistent CRV asymmetric geometries can provide important insights into fundamental characteristics of

243    ONH biomechanics, further systematic studies of the effects of CRV orientations in possible ranges,

244    including normal and pathologic states, would be valuable to reveal the anisotropic properties of ONH

245    biomechanics. Second, the mechanical properties of the ONH components were simplified as a linear elastic

246    material due to limited experimental knowledge. These issues make quantitative evaluation of the

247    mechanical response challenging, and then this study limited qualitative discussion about ONH deformation

248    characteristics against a representative value of mechanical parameters and IOP within normal ranges [30].

249    Following the possible range of material parameters [30], vascular tissue is sufficiently stiffer than neural

250    tissues, and characteristic deformation due to CRVs particularly in the prelamina was constantly found

251    within this range in preliminary analyses. Nevertheless, further systematic studies of the effects of material

252    parameters based on further experimental knowledge would be useful to clarify the ONH deformation

253    states quantitatively and damage risk estimations. In addition, the IOP change does not affect relative ONH

254    deformation states due to its linear elastic assumption, while the CRVs potentially cause nonlinear

255    mechanical responses in the ONH deformation against IOP change, particularly in soft issues such as the

256　prelamina. Related to this issue, *in vivo* mechanical estimations of the subject-specific LC and prelamina

257　from these deformation states have been attempted without considering the CRV [16,37]. However, the

258　results obtained in the present study suggested that the mechanical effects of the CRV might be

259　nonnegligible in this mechanical estimation. To obtain general conclusions about the CRV effects on ONH

260　biomechanics, experimental tests of the material properties of the CRV are required. Third, this is the first

261　study to consider the CRV effects on ONH biomechanics and was limited to cases of healthy subjects. The

262　extent of the CRV effects would be exacerbated in glaucoma patients with mechanically damaged ONH, and

263　thus reasonable modeling of mechanically induced ONH tissue damage in glaucoma progression would give

264　new insight into the mechanical implication of the nasal shift of the CRVs, as observed in glaucoma patients

265　[5].

266　　　In conclusion, this study investigated the effects of 3D asymmetric CRVs on ONH deformation

267　states. The CRV branching morphologies in the ONH were constructed based on the OCT images of eight

268　healthy subjects and superimposed to the axisymmetric idealized ONH geometry. Computational

269　mechanical simulation of the ONH deformation against the IOP exhibited that the CRVs induced anisotropic

270　deformation with a relatively higher strain distribution, particularly in the prelamina, which is relatively soft

271　neural tissue. Although the CRVs in having a relatively stiffer structure were believed to display mechanical

272　support functions against IOP in ophthalmology, the current findings suggested that they induce complex

273　anisotropic deformation with local strain concentrations. These concluding remarks provide new important

274　insights into regional differences of the ONH biomechanical states associated with regional damage of the

275　ONH tissues observed in glaucoma, and thus we hope this study motivates further investigations about CRV

276　mechanical properties and functions in glaucoma patients.

277

278　**Supplementary material**

279　Supplementary material 1: Overview of smoothed finite element method and code verification

280

281　**Acknowledgments**

11

285

286    **Conflicts of Interest statement**

287    The authors declare that the research was conducted in the absence of any commercial or financial

288    relationships that could be construed as a potential conflict of interest.

289

290

**References**

[1]   Quigley HA, Broman AT. The number of people with glaucoma worldwide in 2010 and 2020. Br J Ophthalmol 2006;90:262–7.

[2]   Burgoyne CF, Crawford Downs J, Bellezza AJ, Francis Suh JK, Hart RT. The optic nerve head as a biomechanical structure: A new paradigm for understanding the role of IOP-related stress and strain in the pathophysiology of glaucomatous optic nerve head damage. Progress in Retinal and Eye Research 2005;24:39–73.

[3]   Sigal IA, Ethier CR. Biomechanics of the optic nerve head. Exp Eye Res 2009;88:799–807.

[4]   Campbell IC, Coudrillier B, Ross Ethier C. Biomechanics of the posterior eye: a critical role in health and disease. J Biomech Eng 2014;136:021005.

[5]   Radcliffe NM, Smith SD, Syed ZA, Park SC, Ehrlich JR, De Moraes CG, et al. Retinal blood vessel positional shifts and glaucoma progression. Ophthalmology 2014;121:842–8.

[6]   Varma R, Spaeth GL, Hanau C, Steinmann WC, Feldman RM. Positional changes in the vasculture of the optic disk in glaucoma. American Journal of Ophthalmology 1987;104:457–64.

[7]   Wang YX, Panda-Jonas S, Jonas JB. Optic nerve head anatomy in myopia and glaucoma, including parapapillary zones alpha, beta, gamma and delta: Histology and clinical features. Prog Retin Eye Res 2021;83:100933.

[8]   Panda SK, Cheong H, Tun TA, Chuangsuwanich T, Kadziauskiene A, Senthil V, et al. The three-dimensional structural configuration of the central retinal vessel trunk and branches as a glaucoma biomarker. Am J Ophthalmol 2022;240:205–16.

[9]   Quigley HA, Hohman RM, Addicks EM, Green WR. Blood vessels of the glaucomatous optic disc in experimental primate and human eyes. Investigative Ophthalmology and Visual Science 1984;25:918–31.

[10] Jonas JB, Budde WM, Németh J, Gründler AE, Mistlberger A, Hayler JK. Central retinal vessel trunk exit and location of glaucomatous parapapillary atrophy in glaucoma. Ophthalmology 2001;108:1059–64.

316  [11] Wang B, Lucy KA, Schuman JS, Ishikawa H, Bilonick RA, Sigal IA, et al. Location of the Central Retinal

317      Vessel Trunk in the Laminar and Prelaminar Tissue of Healthy and Glaucomatous Eyes. Sci Rep

318      2017;7:9930.

319  [12] Sawada Y, Araie M, Shibata H, Iwase T. Nasal displacement of retinal vessels on the optic disc in

320      glaucoma associated with a nasally angled passage through lamina cribrosa. Sci Rep 2021;11:1–9.

321  [13] Xin D, Talamini CL, Raza AS, de Moraes CGV, Greenstein VC, Liebmann JM, et al. Hypodense regions

322      (holes) in the retinal nerve fiber layer in frequency-domain OCT scans of glaucoma patients and

323      suspects. Investigative Ophthalmology and Visual Science 2011;52:7180–6.

324  [14] Sigal IA, Flanagan JG, Tertinegg I, Ethier CR. Finite element modeling of optic nerve head biomechanics.

325      Invest Ophthalmol Vis Sci 2004;45:4378–87.

326  [15] Wang X, Rumpel H, Lim WEH, Baskaran M, Perera SA, Nongpiur ME, et al. Finite Element Analysis

327      Predicts Large Optic Nerve Head Strains During Horizontal Eye Movements. Invest Ophthalmol Vis Sci

328      2016;57:2452–62.

329  [16] Sigal IA, Grimm JL, Schuman JS, Kagemann L, Ishikawa H, Wollstein G. A method to estimate

330      biomechanics and mechanical properties of optic nerve head tissues from parameters measurable

331      using optical coherence tomography. IEEE Trans Med Imaging 2014;33:1381–9.

332  [17] Girard MJA, Beotra MR, Chin KS, Sandhu A, Clemo M, Nikita E, et al. In Vivo 3-Dimensional Strain

333      Mapping of the Optic Nerve Head Following Intraocular Pressure Lowering by Trabeculectomy.

334      Ophthalmology 2016;123:1190–200.

335  [18] Zhang L, Thakku SG, Beotra MR, Baskaran M, Aung T, Goh JCH, et al. Verification of a virtual fields

336      method to extract the mechanical properties of human optic nerve head tissues in vivo. Biomech

337      Model Mechanobiol 2017;16:871–87.

338  [19] Mao Z, Miki A, Mei S, Dong Y, Maruyama K, Kawasaki R, et al. Deep learning based noise reduction

339      method for automatic 3D segmentation of the anterior of lamina cribrosa in optical coherence

340      tomography volumetric scans. Biomed Opt Express 2019;10:5832–51.

341   [20] Sato Y, Nakajima S, Shiraga N, Atsumi H, Yoshida S, Koller T, et al. Three-dimensional multi-scale line

342        filter for segmentation and visualization of curvilinear structures in medical images. Med Image Anal

343        1998;2:143–68.

344   [21] McCormick M, Liu X, Jomier J, Marion C, Ibanez L. ITK: enabling reproducible research and open science.

345        Front Neuroinform 2014;8:13.

346   [22] Sigal IA, Flanagan JG, Ross Ethier C. Factors Influencing Optic Nerve Head Biomechanics. Invest

347        Ophthalmol Vis Sci 2005;46:4189–99.

348   [23] Zhang L, Albon J, Jones H, Gouget CLM, Ethier CR, Goh JCH, et al. Collagen microstructural factors

349        influencing optic nerve head biomechanics. Invest Ophthalmol Vis Sci 2015;56:2031–42.

350   [24] Voorhees AP, Jan N-J, Austin ME, Flanagan JG, Sivak JM, Bilonick RA, et al. Lamina Cribrosa Pore Shape

351        and Size as Predictors of Neural Tissue Mechanical Insult. Invest Ophthalmol Vis Sci 2017;58:5336–46.

352   [25] Rebhan J, Parker LP, Kelsey LJ, Chen FK, Doyle BJ. A computational framework to investigate retinal

353        haemodynamics and tissue stress. Biomech Model Mechanobiol 2019;18:1745–57.

354   [26] Mitchell P, Leung H, Wang JJ, Rochtchina E, Lee AJ, Wong TY, et al. Retinal vessel diameter and open-

355        angle glaucoma: the Blue Mountains Eye Study. Ophthalmology 2005;112:245–50.

356   [27] He ZC, Li GY, Zhong ZH, Cheng AG, Zhang GY, Liu GR, et al. An edge-based smoothed tetrahedron finite

357        element method (ES-T-FEM) for 3D static and dynamic problems. Comput Mech 2013;52:221–36.

358   [28] Cazes F, Meschke G. An edge-based smoothed finite element method for 3D analysis of solid

359        mechanics problems. Int J Numer Methods Eng 2013;94:715–39.

360   [29] Zeng W, Liu GR. Smoothed Finite Element Methods (S-FEM): An Overview and Recent Developments.

361        Arch Comput Methods Eng 2018;25:397–435.

362   [30] Hua Y, Voorhees AP, Sigal IA. Cerebrospinal Fluid Pressure: Revisiting Factors Influencing Optic Nerve

363        Head Biomechanics. Invest Ophthalmol Vis Sci 2018;59:154–65.

364   [31] Krupin T, Liebmann JM, Greenfield DS, Ritch R, Gardiner S. A Randomized Trial of Brimonidine Versus

365        Timolol in Preserving Visual Function: Results From the Low-pressure Glaucoma Treatment Study. Am

366        J Ophthalmol 2011;151:671–81.

367 [32] Amelon R, Cao K, Ding K, Christensen GE, Reinhardt JM, Raghavan ML. Three-dimensional

368     characterization of regional lung deformation. J Biomech 2011;44:2489–95.

369 [33] Sawada Y, Araie M, Shibata H. Vertical Position of the Central Retinal Vessel in the Optic Disc and Its

370     Association With the Site of Visual Field Defects in Glaucoma. Am J Ophthalmol 2021;229:253–65.

371 [34] Kiumehr S, Park SC, Syril D, Teng CC, Tello C, Liebmann JM, et al. In vivo evaluation of focal lamina

372     cribrosa defects in glaucoma. Arch Ophthalmol 2012;130:552–9.

373 [35] Tatham AJ, Miki A, Weinreb RN, Zangwill LM, Medeiros FA. Defects of the lamina cribrosa in eyes with

374     localized retinal nerve fiber layer loss. Ophthalmology 2014;121:110–8.

375 [36] Taylor AW, Sehu W, Williamson TH, Lee WR. Morphometric assessment of the central retinal artery

376     and vein in the optic nerve head. Can J Ophthalmol 1993;28:320–4.

377 [37] Zhang L, Beotra MR, Baskaran M, Tun TA, Wang X, Perera SA, et al. In Vivo Measurements of Prelamina

378     and Lamina Cribrosa Biomechanical Properties in Humans. Invest Ophthalmol Vis Sci 2020;61:27.

379

380

381

Table 1 Material parameters of each component of ONH, taken from [30].

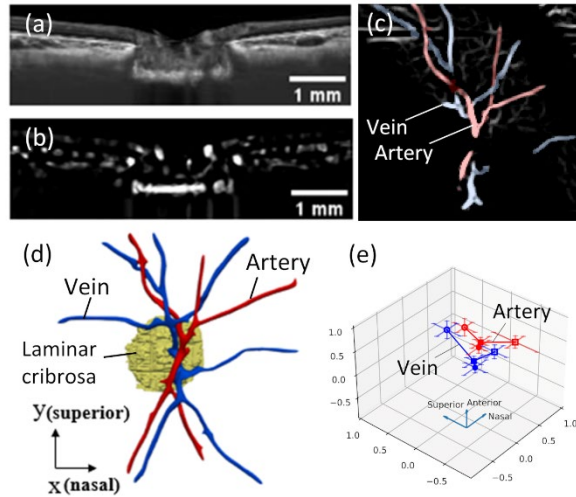| | Young's modulus [MPa] | Poisson's ratio |
|---|---|---|
| Sclera | 9 | 0.49 |
| Central retinal vessels (CRVs) | 5 | 0.49 |
| Lamina cribrosa (LC) | 0.9 | 0.49 |
| Prelamina | 0.09 | 0.49 |
| Retina | 0.09 | 0.49 |

382

**Fig. 1.** Overall workflow to obtain three-dimensional morphologies of the central retinal vessels. Optical coherent tomography images of the optical nerve head (a) were filtered to clarify the blood vessel regions (b), and a single pair of a retinal artery and vein was segmented (c). Central retinal vessels centerlines were extracted, and each root and first and second branch locations were obtained and normalized by the diameter of the lamina cribrosa to avoid subject-specific size differences (d).

**(a) Control**

Lamina cribrosa

Prelamina

Sclera

1.9

Temporal

Nasal

**(b) ONH+CRVs**

2.5

Central retinal vessel

**(c)**

Superior

Temporal

Nasal

LC diameter × 4

Inferior

LC diameter × 4

390

391 **Fig. 2.** Central cross-sectional planes of an idealized axisymmetric optic nerve head (ONH) geometry

392 consisting of the sclera, LC, and prelamina based on [22] (a) and that with embedded central retinal vessels
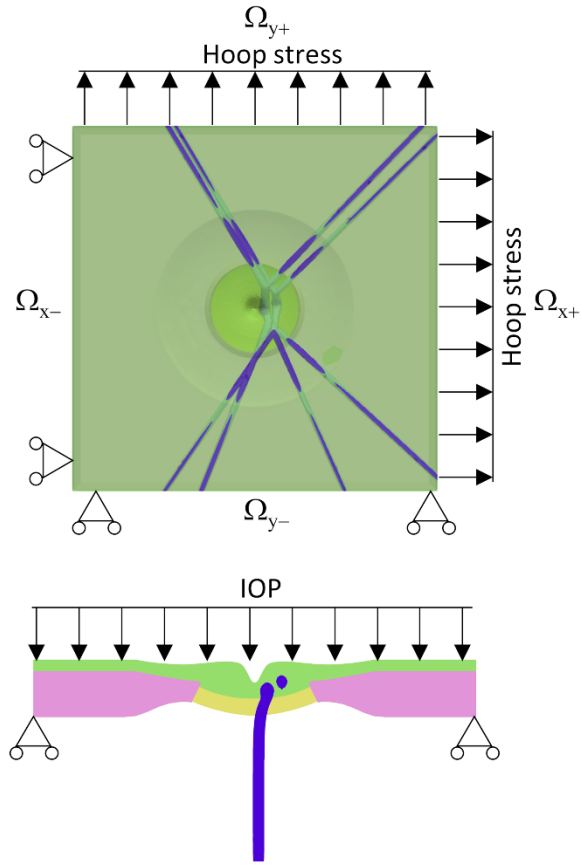
393 (CRVs) (b), and the top view of the ONH with the CRVs (c).

**Fig. 3.** Schematics of the boundary conditions. Intraocular pressure (IOP) was assigned on the top surface of the optic nerve head and associated circumferential (hoop) stress was loaded on the cross-sectional boundary planes. Sliding conditions were set on a pair of cross-sectional boundary planes (temporal and inferior planes, $\Omega_{x-}$ and $\Omega_{y-}$) to constrain the optic nerve head deformation with satisfactory globally symmetric deformation.
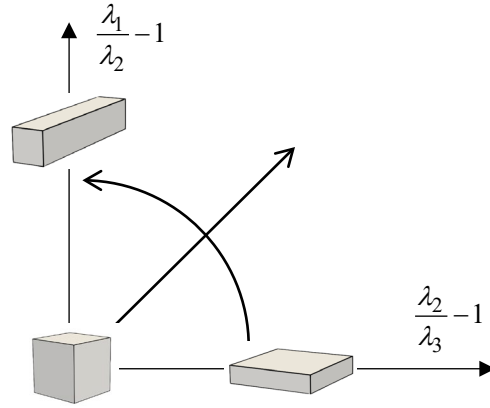
401

402    **Fig. 4.** Schematic of the meanings of the anisotropic deformation index (ADI) and the slab-rod index (SRI)

403    in a case of an incompressible cube, where the principal stretch ratios $\lambda_1 \geq \lambda_2 \geq \lambda_3$ are restricted to
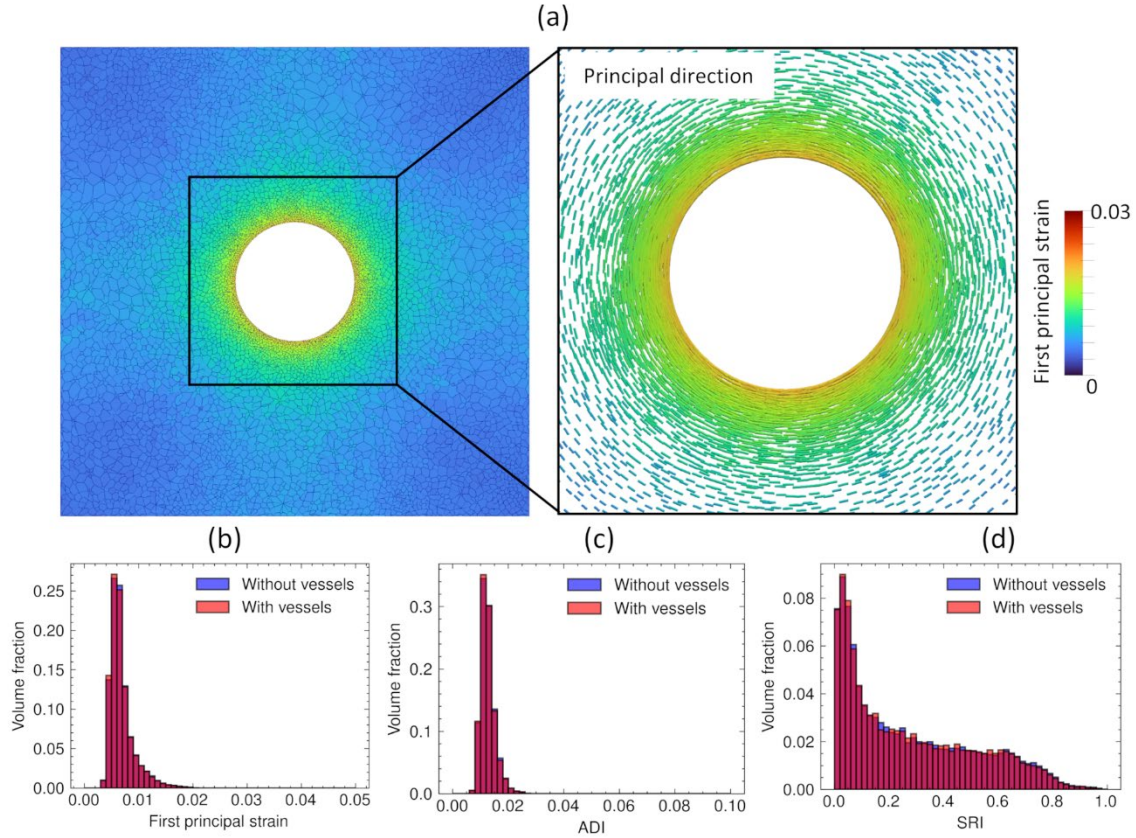
404    $\lambda_1 \lambda_2 \lambda_3 = 1$.

405

406

**Fig. 5.** Spatial distributions of the first principal strain on the cross-sectional plane of the anterior-posterior direction in the sclera (a) and volume fractions of the first principal strain (b), anisotropic deformation index (ADI) (c), and slab-rod index (SRI) (d) in the sclera.
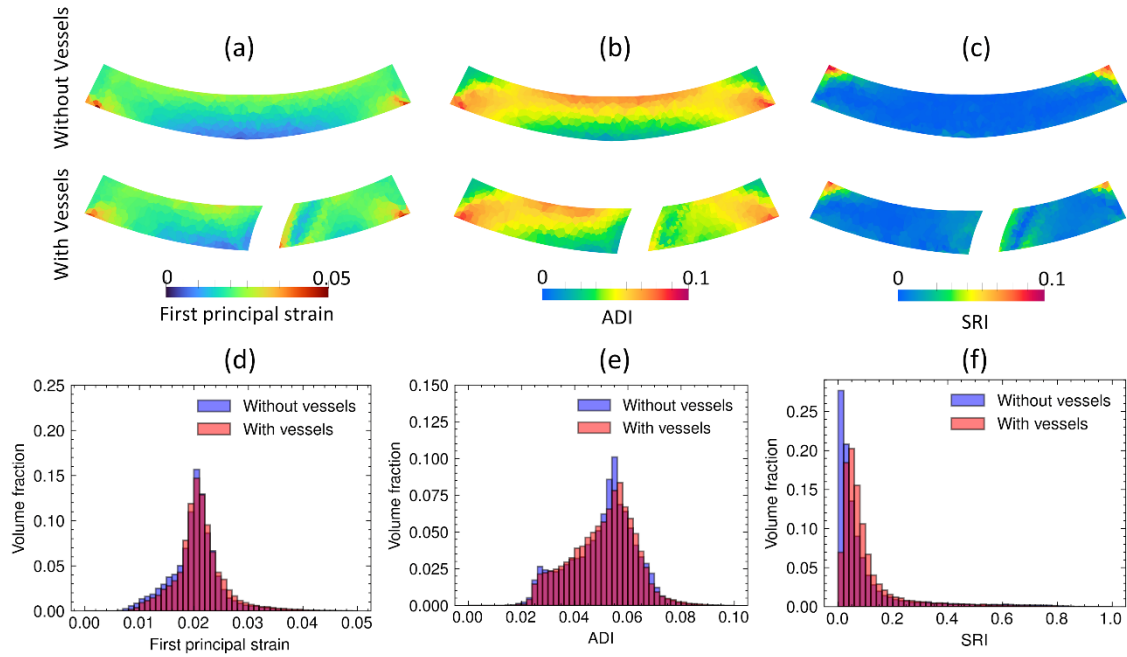
412

**Fig. 6.** Spatial distributions on the central cross-sectional plane of the superior-inferior direction and volume

fractions of the first principal strain (a, d), anisotropic deformation index (ADI) (b, e), and slab-rod index
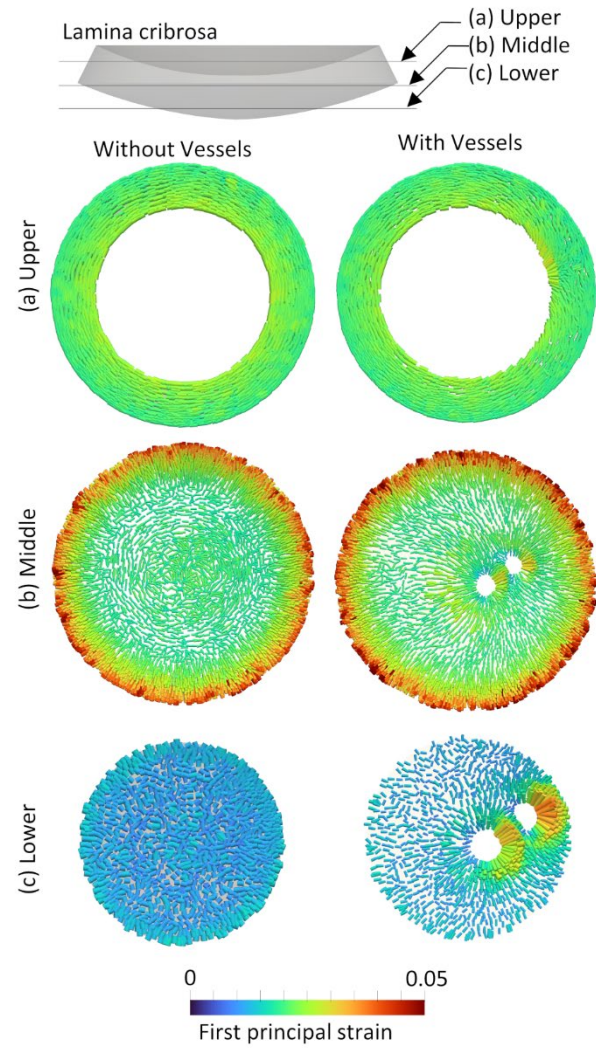
(SRI) (c, f) in the lamina cribrosa.

413

414

415

416

23

**Fig. 7.** Spatial orientations of the first principal strain in the upper (a), middle (b), and lower (c) cross-sectional planes of the anterior-posterior directions without (left) and with vessels (right).
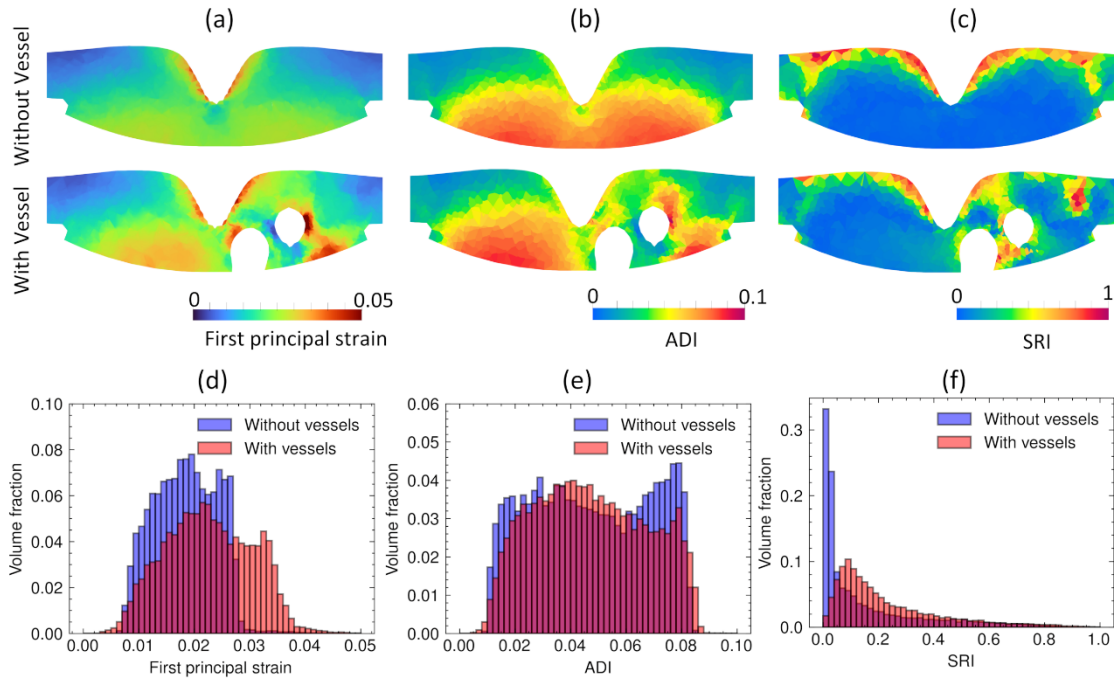
421

Fig. 8. Spatial distributions on the central cross-sectional plane of the superior-inferior direction and

volume fractions of the first principal strain (a, d), anisotropic deformation index (ADI) (b, e), and slab-rod

index (SRI) (c, f) in the prelamina.